PNAS RESEARCH ARTICLE | ENGINEERING

Skin-integrated systems for power efficient, programmable thermal sensations across large body areas

Minsu Park[a,1], Jae-Young Yoo[a,1], Tianyu Yang[a,b,1], Yei Hwan Jung[c,1], Abraham Vázquez-Guardado[a], Shupeng Li[d], Jae-Hwan Kim[a], Jaeho Shin[a], Woo-Youl Maeng[a], Geumbee Lee[a], Seonggwang Yoo[a], Haiwen Luan[a], Jin-Tae Kim[a], Hee-Sup Shin[a], Matthew T. Flavin[a], Hong-Joon Yoon[a], Nenad Miljkovic[b], Yonggang Huang[d], William P. King[b,2], and John A. Rogers[a,d,e,f,g,2]

Contributed by John A. Rogers; received October 21, 2022; accepted December 28, 2022; reviewed by Dae-Hyeong Kim and Sihong Wang

Thermal sensations contribute to our ability to perceive and explore the physical world. Reproducing these sensations in a spatiotemporally programmable manner through wireless computer control could enhance virtual experiences beyond those supported by video, audio and, increasingly, haptic inputs. Flexible, lightweight and thin devices that deliver patterns of thermal stimulation across large areas of the skin at any location of the body are of great interest in this context. Applications range from those in gaming and remote socioemotional communications, to medical therapies and physical rehabilitation. Here, we present a set of ideas that form the foundations of a skin-integrated technology for power-efficient generation of thermal sensations across the skin, with real-time, closed-loop control. The systems exploit passive cooling mechanisms, actively switchable thermal barrier interfaces, thin resistive heaters and flexible electronics configured in a pixelated layout with wireless interfaces to portable devices, the internet and cloud data infrastructure. Systematic experimental studies and simulation results explore the essential mechanisms and guide the selection of optimized choices in design. Demonstration examples with human subjects feature active thermoregulation, virtual social interactions, and sensory expansion.

bioelectronics | virtual reality | wearable

Sensory receptors in the skin define our perceptions of the physical world through various tactile and thermal queues, the essential importance of which was recognized by the 2021 Nobel Prize in Physiology or Medicine (1, 2). Technologies for engaging these receptors in a rapid, programmable fashion with spatiotemporal precision have the potential to greatly enhance experiences in virtual/augmented reality (VR), currently rendered almost exclusively through video and audio inputs. Haptic interfaces to the fingertips and, more recently, across large areas of the body via real-time, wireless control of arrays of miniaturized mechanical actuators have great potential, with application possibilities that span virtual social interactions, entertainment, training, rehabilitation, and remote patient care (3–5). Thermal sensations are also critically important, yet technologies designed to engage thermal receptors in the skin have received comparatively little attention. Some examples include the use of thermal feedback as an alternative to vibrotactile mechanisms in environments where vibratory noise creates confounding effects (6). In others, thermal stimulation can enhance on-screen navigation instructions for sighted users (7), and provide some enhancements to VR spaces (8, 9).

These and related devices for thermal stimulation take the form of accessories, such as rings, wrist-mounted wearables, gloves, earhooks, and anklets (10–15). Significant engineering challenges exist in scaling these simple systems into flexible, large-area platforms that can support programmable arrays of power-efficient actuators, as the basis for full-body sensations. Designs must consider thermal sensitivities that vary across the body (16) and discriminability that depends on the area of stimulation and both the magnitude and rate of change in temperature (17–21). For example, thermal stimulation delivered between 36 °C and 45 °C activates warm thermoreceptors, and below 30 °C activates cold thermoreceptors (22). If the skin temperature rises above 45 °C or falls below 15 °C, activation of nociceptors causes the sensation of pain (23). Thermoelectric modules such as those comprised of bismium-telluride-based thermoelectric pellets, thermally conductive copper (Cu) plates, and dielectric ceramic substrates (24) provide one set of options, but their thick geometries and rigid mechanical properties create difficulties in using them as the basis for thin, soft, and comfortable interfaces to the skin. Recent efforts to address these shortcomings exploit thin, flexible Cu electrodes and soft, silicone composite materials (8, 25). Remaining drawbacks are in requirements for large batteries (8) or external power supplies (25) to support operation, due to the limited power-efficiencies of these systems, and in the need for wired-based interfaces for control (8, 25).

Significance

Growing interest in remote social interactions and in virtual experiences motivates work on engineering systems that can provide real-time, computer-controlled multisensory engagements. Well-developed systems provide realistic audio and video inputs, but without capabilities in stimulating sensory receptors in the skin. Recent research prototypes support pixelated haptic interfaces to mechanoreceptors, in versions that can apply not only to the fingertips but also across large areas of the skin at nearly any location of the body. Devices to create corresponding thermal sensations are comparatively underexplored, but have strong potential to qualitatively expand the overall sensory experience. Here, we report a set of ideas in programmable thermal interfaces to the skin, with examples in active thermoregulation, virtual social interactions, and remote sensory perception.

Reviewers: D.-H.K., Seoul National University; and S.W., University of Chicago.

The authors declare no competing interest.

[1]M.P., J.-Y.Y., T.Y., and Y.H.J. contributed equally to this work.

[2]To whom correspondence may be addressed. Email: wpk@illinois.edu or jrogers@northwestern.edu.

This article contains supporting information online at https://www.pnas.org/lookup/suppl/doi:10.1073/pnas.2217828120/-/DCSupplemental.

Published January 30, 2023.

Here, we report a set of ideas in passive cooling mechanisms, thermally switchable interfaces, and wireless, stretchable electronics platforms as foundations for a technology that can provide power-efficient, programmable patterns of thermal stimulation across large areas of the skin, with closed-loop control. The thin, flexible, and lightweight features of the system support a variety of skin-interfaced form factors, applicable to multiple, large and small areas of the body. Experimental measurements and computational simulations define all of the underlying mechanisms, to guide optimized choices in materials and design layouts. System level examples demonstrate capabilities in three representative applications, 1) active thermoregulation, as a basic but essential function in thermal therapy through comfortable interfaces to the skin across various regions of the body; 2) long-range delivery of spatiotemporal patterns of heating and cooling controlled through multichannel wireless communications between sets of users; and 3) real-time thermal sensory recognition of remote objects through inputs derived from images collected using an infrared (IR) camera.

Results

System Architecture. The ability to generate complex, spatiotemporal patterns of thermal sensation across large areas of the skin demands thin, soft, flexible systems with power-efficient, electronically programmable operation. Fig. 1 shows a representative device, which we refer to here as a thermally controlled epidermal VR (t-eVR) system that addresses these requirements, in a wireless form for convenient, tether-free use. The exploded view schematic illustration highlights the structure, which includes 1) a thin layer of silicone to encapsulate the top surface; 2) a set of thermal modules to enable power-efficient heating and cooling, each with an integrated thermistor; 3) a sheet of flexible electronics to distribute power and closed-loop feedback control signals to the thermal modules; and 4) a thin layer of silicone to encapsulate the top surface (Fig. 1*A*). The electronics platform consists of a multilayer flexible printed circuit board (fPCB) that supports resistive Joule heaters in the form of thin, serpentine Cu traces in fractal geometries and thermistors, along with associated control circuits, surface mount electronic components, a pair of contact pads for a battery, and a coil for wireless charging. Details on the design and the dimensions of each layer appears in *SI Appendix,* Fig. S1.

Each of these heaters integrates with a thin, passive cooling gel and a unique, switchable type of thermal barrier (STB) in a layered configuration to define a thermal module. Fig. 1*B* illustrates the operation in a way that highlights the role of the STB, which consists of a thin bladder formed from a pair of aluminized ethylene-vinyl alcohol (EVOH) films (12 μm thick) that houses a small volume (30 μL) of a liquid with a low boiling point (1-methoxyheptafluoropropane; boiling point of 34 °C at 1 atm). (Design considerations appear in *SI Appendix,* Figs. S2 and S3 and Supporting Text 1). In the cooling mode, the heater is off, and the thin geometry of this bladder in its condensed state supports efficient thermal coupling between the skin and the cooling gel, which operates based on evaporation of water in a super-absorbent polyacrylate (26, 27) (*SI Appendix,* Fig. S4). Under ambient indoor conditions, the skin temperature reaches a spatially uniform value of ~27 °C under these conditions at thermal equilibrium. This temperature coincides with the maximum sensitivity of cutaneous cold receptors (17), thereby creating an effective cooling sensation.

Activating the heater, as described in detail in *SI Appendix,* Fig. S5, vaporizes the liquid and thereby expands the bladder to create a thermal barrier structure that isolates the cooling gel from the skin. The effectiveness of this barrier follows from its thick geometry after expansion and from the low thermal conductivity of the vapor (*SI Appendix,* Fig. S6). As a result, the heating mode can raise the temperature of the skin to a target value (>35 °C) quickly (~5 s) and with relative power efficiency (~1.1 W under ambient conditions). The consequent activation of cutaneous warm receptors (17) creates a warming sensation. Fig. 1*C* shows photographs of a representative heater, which consists of Cu traces (width: 60 μm) in 2 × 2 arrangements of 3rd order Peano curves (28), distributed across an area of 14.4 × 14.4 mm^2. Finite element analysis (FEA) illustrates the uniformity of the temperature distribution that results from passing current through these traces (Fig. 1*D* and *SI Appendix,* Fig. S7). The IR images in Fig. 1*E* show corresponding temperatures that result from the cooling (*Left*) and heating modes (*Right*). A proportional-integral-derivative (PID) controller programmed in the system maintains a constant temperature of the skin at a target value (*SI Appendix,* Fig. S8), based on readings from the integrated thermistor. Appropriate choices for each gain value (k_p = 20, k_i = 0.5, and k_d = 6.0) in the controller ensure a well behaved transient response in temperature rise (*SI Appendix,* Fig. S9). The system exhibits high accuracy in temperature control, with deviations of only up to 1% from the set point (*SI Appendix,* Fig. S10).

A photograph of a device in a bent geometry (Fig. 1*F*) illustrates its flexibility. FEA results (*SI Appendix,* Fig. S11) indicate that the strains in the Cu remain below the yield strain (0.3 %) for a range of deformations such as bending and twisting, to levels relevant for mounting on various body locations. In practice, deformations (bending, etc.) during the heating and cooling process (e.g., bending the thermal module with a finger) have a negligible effect on the temperature control (*SI Appendix,* Fig. S12). The entire system weighs 23.5 g (without battery), and the total thickness is less than 3.5 mm, to facilitate comfortable use on areas such as the chest, back, forearm, and abdomen (Fig. 1*G*). The example shown here includes 16 (4 × 4) independently controlled, thermal modules each with a size of 207.4 (14.4 × 14.4) mm^2, separated by an edge-to-edge distance of 5 mm, covering an area of ~5,221 mm^2. These choices in layout consider the anatomy and responsiveness of thermoreceptors across areas of the body mentioned above. For example, warm and cold receptors on the forearm exist at densities of 0.3 to 0.4 and 6 to 7.5 per cm^2, respectively (29), consistent with two-point discrimination tests (*SI Appendix,* Fig. S13 *A–C*) that indicate values of ~13 cm for heating and ~7 cm for cooling (*SI Appendix,* Fig. S13*D*). Thresholds for experiencing warm sensations and for discriminating differences in elevated temperatures are both approximately +1.5 °C for thermal stimulation over areas of 200 mm^2 (21).

Passive Cooling and Thermal Switching Mechanisms. The STB and the cooling gel are both critically important for power-efficient operation. Experiments that use different combinations of cooling gel, STB, and heater on a skin phantom in open air, as illustrated in Fig. 2*A* and summarized in *SI Appendix,* Fig. S14 and Table S1, isolate the role of each component. Case I corresponds to the complete module, with all three components. Case II includes only the STB and heater, such that thermal transport to the surrounding air represents the only cooling mechanism. Case III includes only the cooling gel and the heater, thereby eliminating the benefits of the STB. Case IV is a structure only with a heater, as a reference. A temperature sensor located underneath the heater and in direct contact with the skin phantom yields an estimate of the temperature at the surface of the skin (T_{skin}), assuming that the heater has a negligible thermal impedance (~10 mm^2 K W^{-1}) compared with other components.

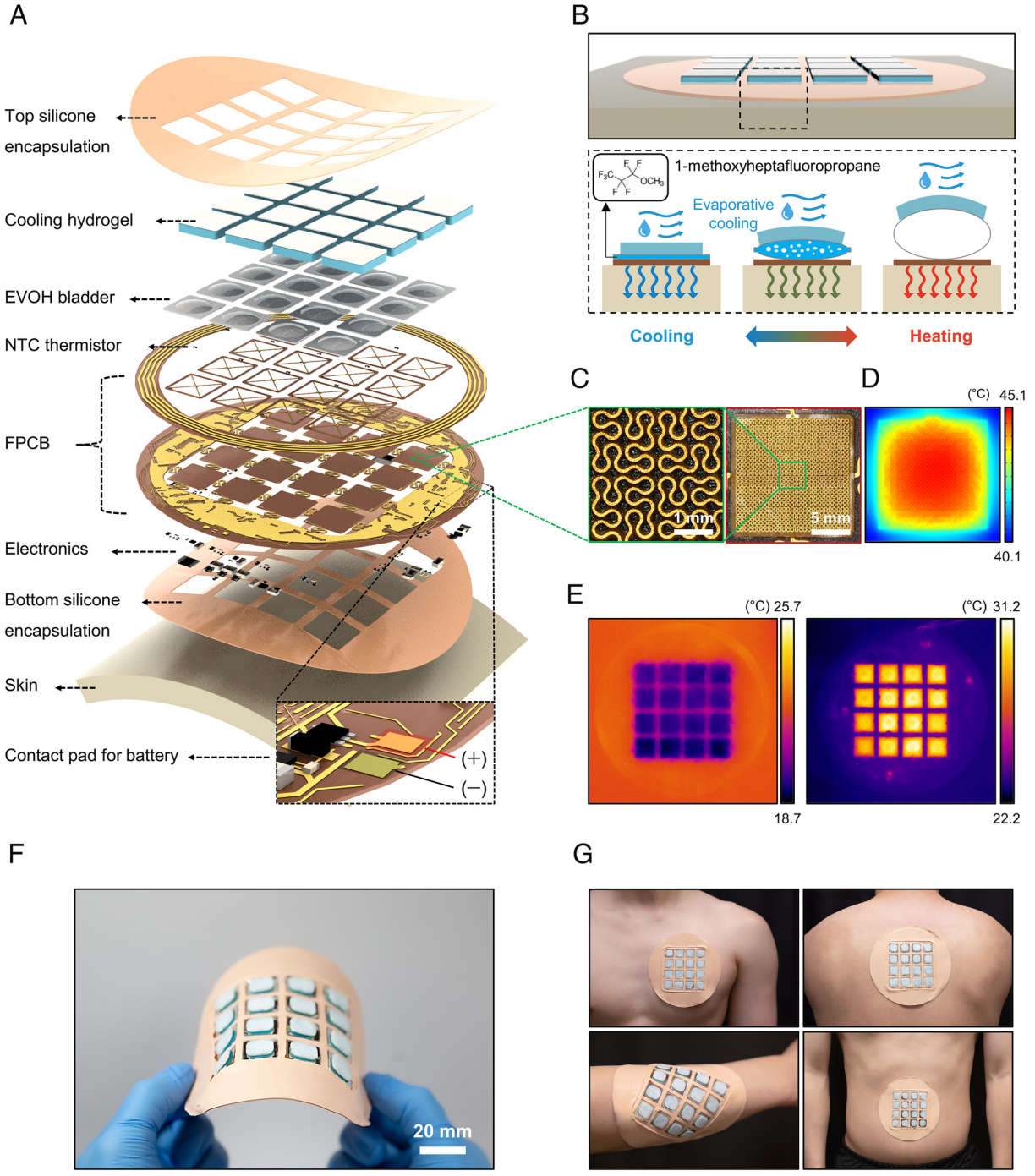

Fig. 1. Design of a thin, flexible, wireless system for generating programmable patterns of thermal sensation across large areas of the skin. (*A*) Exploded view schematic illustration of a device with 16 independently controlled thermal modules. Each module includes a flexible heater, a negative temperature coefficient (NTC) thermistor, an expandable bladder (as a STB), and a cooling hydrogel. (*B*) Schematic illustration of the working principle of the device at the skin interface. (*C*) Photographs of a flexible heater based on Cu traces in a space-filling Peano fractal geometry. (*D*) FEA simulation result for Joule heating, illustrating a uniform temperature distribution. (*E*) Infrared (IR) images of a device during the cooling (*Left*), and heating (*Right*) mode of operation. (*F* and *G*) Photographs of the device (*F*), and thermal interfaces at various body locations, such as chest, back, forearm, and abdomen (*G*).

Measurements of the power required to reach a defined skin temperature in a fixed period of time serve as the basis for comparisons. Fig. 2*B* shows that an increase in T_{skin} by $\Delta T \approx 13$ °C (from 27 °C to 40 °C) within 7 s (≈1.86 °C s^{-1}) requires applied voltages of 5.0, 4.4, 8.2, and 3.9 V for cases I, II, III, and IV, respectively. This rate of increase is a useful benchmark because it allows the user to detect changes in skin temperature of less than 0.5 °C, starting from the natural temperature of the skin (32 °C) (17). As this rate decreases, the minimum detectable change in temperature increases significantly. For example, at a rate of less than 0.05 °C s^{-1}, the detectable change is ~3 °C (21). The average power and total energy values appear in Fig. 2 *C* and *D* and *SI Appendix*, Fig. S15. As expected, the power and the energy consumption for case III are the largest (~2.9 W, and ~21 J, respectively), simply because the cooling gel counteracts the effects of Joule heating. For case I, activation of the STB isolates the cooling gel from the heater and underlying skin, thereby significantly reducing the power and the energy consumption (~1.2 W and

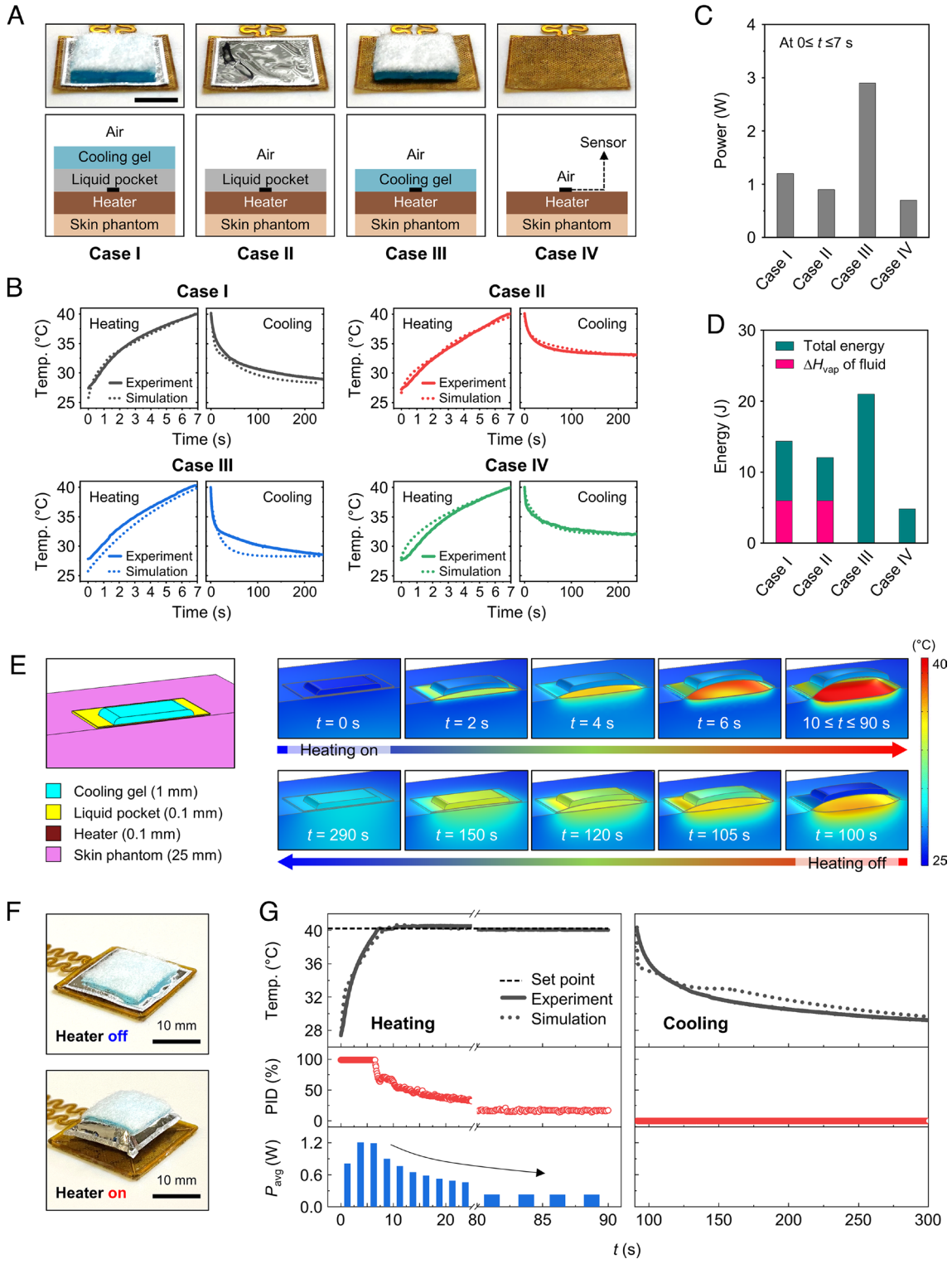

Fig. 2. Mechanisms of thermal switching. (*A*) Photographs (*Top*) and cross-sectional illustrations (*Bottom*) for four different thermal module designs based on a combination of cooling gel, an expandable bladder (as a STB), and a heater on a skin phantom. Case I consists of a cooling gel, STB, and heater. Case II consists of an STB and heater. Case III consists of a cooling gel and heater. Case IV consists of a heater only. In each case, the top and bottom surfaces contact with the ambient air and the skin phantom (Sylgard 184), respectively. (Scale bar: 5 mm.) (*B*) Temperature profile for heating and cooling in each case. (*C* and *D*) Average power ($0 \le t \le 7$ s) for inducing $\Delta T \approx 13$ °C (*C*), and total energy consumption ($0 \le t \le 7$ s) (*D*) for each case. (*E*) 3D model of a half of a thermal module (Case I) and FEA simulation results that show inflation/deflation of the STB with the heater on and off. (*F*) Photographs of the thermal module with the heater off (*Top*) and on (*Bottom*). (*G*) Temperature profile, PID value, and average power consumption of a thermal module operating in both heating and cooling modes.

~8.4 J, respectively). Vaporization of the liquid consumes some energy, estimated as ~5.9 J (for 30 μL, ΔH_{vap} = 142 kJ kg^{-1}). For case II, the absence of the cooling gel further lowers the power (~0.9 W) and the energy (~6.1 J) consumption, but only by a modest amount compared with case I, as evidence of the efficiency and effectiveness of the STB. The simplest structure, case IV, has the lowest power (~0.7 W) and lowest energy (~4.8 J) consumption, as expected, but still within a factor of two of the complete

thermal module, case I. The results also indicate that different combinations of components lead to different rates of temperature increase during heating. Another set of comparison experiments involves application of a fixed power (≈0.6 W) to induce a similar change in T_{skin} ($\Delta T \approx 13$ °C, from 27 °C to 40 °C) (*SI Appendix,* Figs. S16 and S17). Consistent with expectation, the times to reach this change are ~32 s, ~13 s, ~89 s, and ~9 s for cases I, II, III, and IV, respectively.

Unlike active cooling components such as Peltier devices, the cooling gel consumes no electrical power. The cooling performance can be determined by monitoring the decrease in temperature after heating to 40 °C (Fig. 2*B*). For cases I and III, the T_{skin} reaches the base temperature (≈32 °C, $\Delta T = -8$ °C) within 60 s, whereas the corresponding times for cases II and IV are larger than 180 s. Upon cooling, condensation in the STB releases heat, which reduces the cooling rate for case I compared with case III, and for case II compared with case IV. In cases I and III, an additional reduction in temperature occurs until the temperature reaches the initial value (≈27 °C, $\Delta T = -13$ °C) determined by action of the cooling gel. These results indicate that case I, which incorporates the cooling gel and STB, is the most energy efficient structure for both heating and cooling.

Additional studies define the specific cooling power of the cooling gel ($\dot{q}_{cooling}$) in case I as a function of T_{skin}, the temperature of the skin phantom before application of the gel, v_{air}, the speed of airflow in the ambient, relative humidity (*RH*), and temperature (T_{air}) of ambient air (*SI Appendix,* Figs. S18–S21 and Supporting Text 2). Under the condition of free convection (v_{air} = 0 m s^{-1}), when the T_{skin} is 25.9, 29.1, 32.0, 35.1, 38.8, and 41.7 °C, the values of $\dot{q}_{cooling}$ are 290 ± 30, 320 ± 20, 330 ± 10, 370 ± 30, 400 ± 10, and 450 ± 30 W m^{-2}, respectively, consistent with a linearly proportional relationship (*SI Appendix,* Fig. S21*A* and Table S2). For cases of forced convection with different airflow velocities (v_{air} of ~0.2, ~0.6, ~1.0, and ~1.3 m s^{-1}), the values of $\dot{q}_{cooling}$ when T_{skin} = 32.0 °C, are 620 ± 20, 710 ± 30, 750 ± 60, and 790 ± 60 W m^{-2}, respectively (*SI Appendix,* Fig. S21*B* and Table S3). For other cases of forced convection (v_{air}≈1.3 m s^{-1}) with different RH of ambient air (*RH* of 20, 40, and 60 %), the values of $\dot{q}_{cooling}$ when T_{air} = 25.0 °C, are 1,100 ± 40, 880 ± 40, and 690 ± 20 W m^{-2}, respectively (*SI Appendix,* Fig. S21*C* and Table S4). Under the condition of fixed v_{air}≈ 1.3 m s^{-1} and *RH* = 40 %, the values of $\dot{q}_{cooling}$ are 660 ± 10, 720 ± 70, 880 ± 40, 940 ± 20, and 1,100 ± 10 W m^{-2} when the T_{air} is 15, 20, 25, 30, and 35 °C, respectively (*SI Appendix,* Fig. S21*D* and Table S5). The working lifetime of the cooling gel is approximately ~5.7 h if the heater is not activated. Activating the heater will reduce this time due to accelerated evaporation of water (*SI Appendix,* Fig. S21*E*). The values of $\dot{q}_{cooling}$ measured in this study are similar to those determined for other cooling hydrogels in previous reports (30).

Fig. 2*E* summarizes results of three dimensional (3D) FEA of operation of the thermal module during heating and cooling. The cross-sectional images highlight the thermomechanical deformations and temperature distributions as a function of time. Initially, the temperature is below that of the boiling point of liquid in the STB. Here, the thin geometry and relatively high thermal conductivities of the liquid and the materials that define the bladder enable efficient conduction of heat from the skin to the cooling gel. Increases in the temperature lead to vaporization of the liquid and expansion of the bladder, thereby activating the STB (*SI Appendix,* Fig. S22). The relatively low thermal conductivity of the vapor (k_{vapor}) and the greatly increased thickness of the bladder (t_{pocket}) create a thermal barrier that isolates the cooling gel from the skin ($R_{switch} \approx t_{pocket}/k_{vapor}$). The thermal barrier confines heat generated by the heater to the skin, thereby enhancing the efficiency by eliminating parasitic pathways for heat transfer. The cooling operation begins after 90 s, upon deactivation of the heater. The inner pressure of the bladder decreases with temperature, thereby reducing its thickness and enhancing the efficiency of heat conduction through it, until the vapor completely condenses, to reach the off state of the STB. The system does not consume power during this process, due to the passive, evaporative cooling provided by the gel. Photographs in Fig. 2*F* show the thermal switching module during activation and deactivation of the heater. Fig. 2*G* summarizes experimental and simulated results for heating and cooling. The skin reaches the target temperature of 40 °C in 7 s with a power consumption of ~1.2 W. Due to the action of the STB, the power consumption required to maintain the skin temperature at 40 °C continuously decreases after 7 s, and remains at a constant, low level of ~0.2 W after approximately 80 s. Differences in dimensions of the bladder influence the thermal switching efficiency. Details of results appear in *SI Appendix,* Figs. S23 and S24 and Supporting Text 3.

An important benchmark follows from simulations of an ideal situation in which heating and cooling occur at the surface of the skin as before (Fig. 2*B*) but with a system that eliminates all mechanisms for parasitic heat loss and with actuators that have zero thermal mass (*SI Appendix,* Fig. S25*A*). Under these assumptions, the power required for increasing T_{skin} by $\Delta T \approx 13$ °C (from 27 °C to 40 °C) within 7 s, is ~0.5 W; that for decreasing T_{skin} by $\Delta T \approx -8$ °C (from 40 °C to 32 °C) within 60 s is ~0.04 W (*SI Appendix,* Fig. S25 *B–E*). The corresponding energy required to cycle the skin temperature by heating and then cooling using an optimized module with the same parameters is ~14 J, which is only a factor of ~2.4 higher than the ideal case. Reducing the thermal mass of thermal module can further reduce that energy to a value within a factor of ~1.5 of the ideal case (*SI Appendix,* Fig. S25 *F* and *G*).

Circuit Design and Operating Principles. Fig. 3*A* presents a circuit and block diagram of a complete system, with wireless feedback control. A Bluetooth low-energy system on a chip (BLE SoC) with custom firmware provides logic to control the operation state of the heater in each thermal module through a set of 16 general-purpose input/output (GPIO) pinouts. Thermistors at the top surface of each heater (facing the liquid pocket) provide (*SI Appendix,* Fig. S26) measurements of temperature as the basis for feedback control using a PID process operating at a sampling rate of 100 Hz. The duty cycle of a pulse-width modulation signal generated from the GPIO determines the power delivered to each heater. A duty cycle of 100% allows rapid heating to reach a given temperature set point, after which the duty cycle decreases to maintain this value. The set point for each thermal module passes from a mobile device to the BLE SoC and corresponding temperature values wirelessly pass from the BLE SoC to the device, both via standard communication protocols. A cloud server enables control of thermal modules (Fig. 3 *B*, *Left*) and/or sharing of temperature measurements (Fig. 3 *B*, *Right*) at any location with internet access.

In this way, the t-eVR device supports real-time spatiotemporal control of patterns of heating/cooling (Fig. 3*C* and *SI Appendix,* Fig. S27). Fig. 3*D* shows an example of switching between different areas of heating/cooling, from 2.1 cm^2 to 33.2 cm^2. Literature reports indicate that as the stimulation area increases from 2 cm^2 to 14 cm^2, the thermal threshold for sensation on the forearm decreases from 1.5 °C to ~0.2 °C (21). Perception tests for heating over areas of 2.1, 8.3, 18.7, and 33.2 cm^2 by operating 1, 4, 9, and 16 heaters, respectively, indicate that the average perception accuracy on the forearm is 75.0, 75.7, 75.9, and 81.8 %, respectively (Fig. 3*E*).

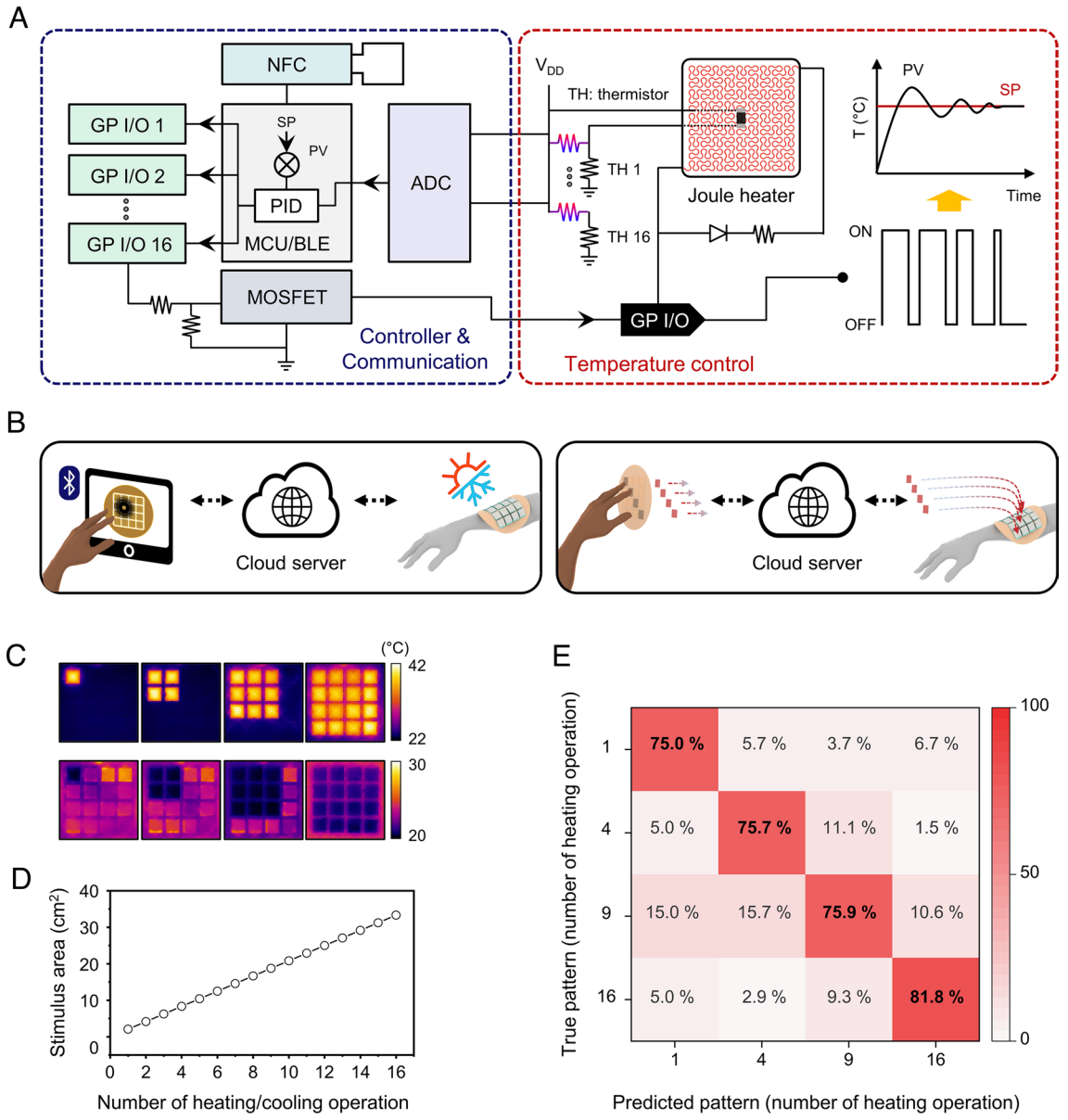

Fig. 3. Operating principles and examples in remote thermal interactions. (*A*) Circuit and block diagram of wireless feedback control. NFC, near-field communication; SP, set point; PV, process value; PID, proportional-integral-derivative; MOSFET, metal-oxide-semiconductor field-effect transistor; ADC, analog-to-digital converter. (*B*) Scheme for two types of operation: touchscreen to device (*Left*) and device-to-device (*Right*), both through cloud server communication. (*C*) IR images of the device in two thermal modes when 1, 4, 9, and 16 thermal modules are in heating (*Top*) or cooling (*Bottom*) operation. (*D*) Stimulus area (cm^2) according to the number of thermal modules in operation. (*E*) Confusion matrix result for 250 blind tests of perception accuracy for different stimulation areas. The number of thermal modules during heating operation (1, 4, 9, and 16) corresponds to thermal stimulation over areas of 2.08, 8.33, 18.7, and 33.3 cm^2, respectively.

On-Body Thermoregulation. Thermoregulation is a basic feature of homeostasis, in which the body maintains a core temperature of ~37 °C (31). The large areas (>33 cm^2) of the systems reported here and their ability to form comfortable thermal interfaces across various regions of the body suggest capabilities in thermoregulation that exceed those of previous devices for uniform heating/cooling by use of thermoelectric elements [16 cm^2 (32) and 25 cm^2 (25)]. Fig. 4*A* shows photographs of operation in this mode, through thermal interfaces formed on the inner surfaces of stretchable compression shirts and leggings (Spandex; polyether-polyurea copolymer) at the chest, back, abdomen, lower arm, and thigh. For infants, where assisted thermoregulation is an essential aspect of patient care, the device can cover almost the entire area of the back (Fig. 4 *B* and *C*). By comparison to control of the ambient temperature, this scheme is attractive because regulation occurs directly through the skin.

Additional demonstrations involve a volunteer with an inactive device on the left arm and an active device on the right arm, the latter operated by PID feedback control to a set point of ~32 °C. As expected, the temperature, T_{skin}, of the left arm remains at a constant value (~32 °C) while indoors, but decreases when outdoors in cold (T_{air} ~ 13 °C) weather (blue line, Fig. 4*D*). The right arm remains at the set point throughout (green line, Fig. 4*D*). Similar behaviors occur under indoor and outdoor conditions in hot weather (T_{air} ~ 35 °C) (Fig. 4*E*). Moreover, the thermoregulating performance of the system also operates well at even lower (T_{air} ~ 5 °C) or higher (T_{air} ~ 45 °C) ambient temperatures based on the tests in an environmental chamber (*SI Appendix*, Fig. S28 and Supporting Text 4).

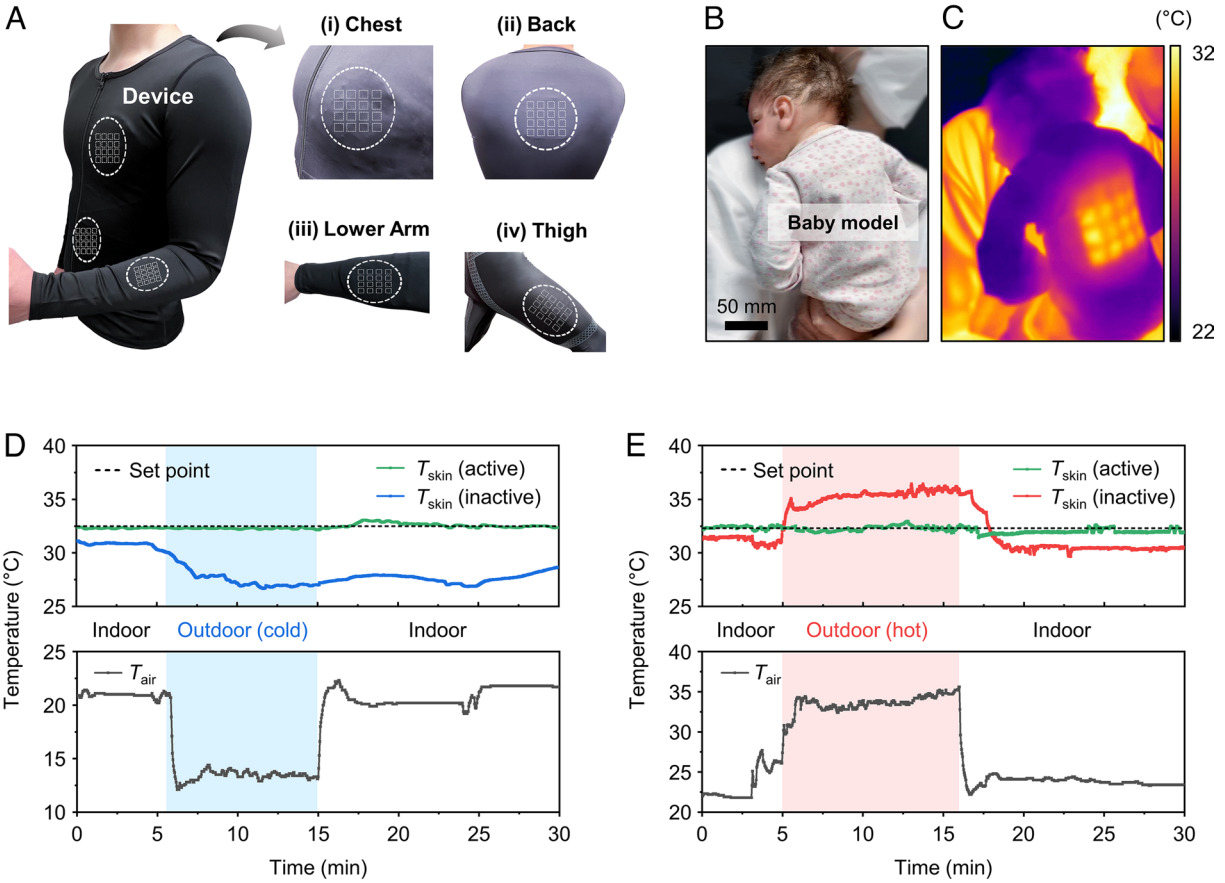

Fig. 4. Programmable, on-body thermoregulation. (*A*) Photographs of thermal interfaces to the inner sides of a stretchable compression shirt and leggings at the chest, back, abdomen lower arm, and thigh. (*B* and *C*) Photograph (*B*), and IR image (*C*) of a baby model with a device on the back. The temperature of the back is actively maintained at 32 °C by PID-control. (*D* and *E*) Change of skin temperature (T_{skin}) in cold weather (T_{air} ≈ 13 °C) (*D*), and hot weather (T_{air} ≈ 35 °C) (*E*) with the system on/off on the forearm.

Long-Range Delivery of Spatiotemporal Thermal Pattern. These t-eVR systems can also be used to enhance remote social interactions through thermal sensations. Previous reports based on thermoelectric devices with comparatively simple designs, hardwired connections, and high power consumption indicate that this mode of interaction can augment perceptions of text and voice messages (7, 33, 34). Fig. 5*A* illustrates an example of a thermal pattern detected by a device operated by user A and transmitted to a device worn by user B. In this example, one device supports sensing and transmission of temperature distributions created by the touch of fingertips (at location 1), and the other reproduces this temperature information at a separate location (at location 2, ~20 km apart) (Fig. 5*B*). Fig. 5*C* shows the position of each heater in the device and three different spatiotemporal thermal patterns sequentially transmitted from location 1. As shown in Fig. 5*D*, each pattern corresponds to touch for ~30 s. For example, pattern #1 (position of thermal modules: 4, 7, 10, and 13) corresponds to 30 s after initiation of a first pattern of touch, followed by release for 60 s, and similarly for pattern #2 (positions: 1, 6, 11, and 16) and pattern #3 (positions: 6, 7, 10, and 11) (Movie S1). The sequence of thermal IR images of the device at location 1, and the corresponding temperature profiles for each thermal module at location 2 confirm the operation (Fig. 5 *E* and *F*). This same scheme can be easily extended to many users.

Sensory Expansion for Thermal Recognition of Remote Objects. Another application is in enhanced somatosensory perception by use of information obtained from thermal images to control patterns of thermal stimulation (Fig. 6*A*). In this demonstration, a portable IR imaging system provides the basis for sensing distributions of temperature across a remote object, as a mechanism, for example, to avoid burns. The imaging information passes wirelessly to a skin-interfaced device to control its operation, as illustrated in the flow chart of Fig. 6*B*. Specifically, a thermal image at a resolution of 160 × 120 pixels captured using a mobile IR camera (FLIR ONE pro, FLIR Inc.) defines a repixelated rendering at 4 × 4 pixels, in real-time. The average temperature of each pixel defines set points for a corresponding set of thermal modules, mounted at a desired location of the body. Notional examples of this form of remote temperature sensing in the context of laboratory safety appear in Fig. 6 *C*–*N* and Movie S2, for cases of an overheated laptop computer, a hot soldering iron and an exothermic chemical reaction. Details appear in the *SI Appendix,* Supporting Text 5.

Discussion

The systems reported here are most notable for their use of ideas in passive mechanisms for cooling and switchable thermal barrier (STB) control. Integrating resistive heating elements, closed-loop wireless electronics, and internet/cloud support yields devices that enable real-time, spatiotemporal control of patterns of heating and cooling, with wide-ranging capabilities in thermal sensory inputs, to complement those based on video, audio, and haptic mechanisms. The approach can support full-body coverage, with magnitudes and rates of temperature change that allow engagement

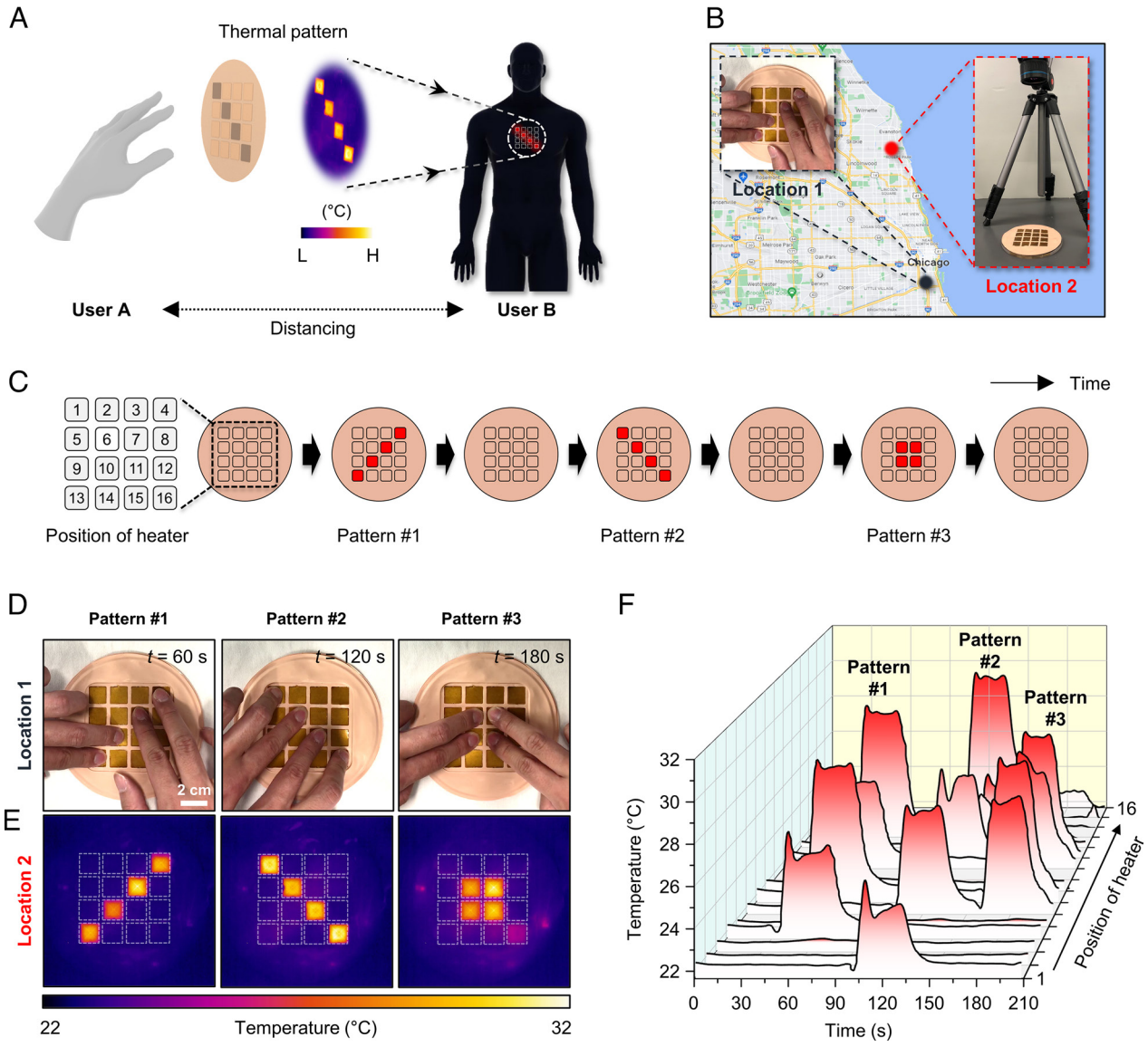

Fig. 5. Remote delivery of spatiotemporal patterns of thermal sensation. (*A*) Conceptual illustration of thermal mirroring enabled by device-to-device communication between users at separate locations. (*B*) Measurement setup at two locations (~20 km apart). At location 1, a pattern of finger touch defines a corresponding spatiotemporal pattern of temperature on a device at this location. At location 2, the temperature information transmitted from location 1 is reproduced in real-time at a device at this location, as measured using an IR camera. (*C*) Thermal pattern sequence at location 1. Each pattern is applied for ~30 s and then released. (*D*) Photographs of patterns of touch #1~3 applied to the device at location 1. (*E*) IR images of corresponding thermal patterns #1~3 produced by the device at location 2. (*F*) Temperature profiles of spatiotemporally delivered thermal patterns measured at location 2.

of thermoreceptors in the skin at nearly any location of the body. Beyond demonstrated applications in thermoregulation, social interactions and sensory expansion, additional opportunities are in gaming, entertainment, training, rehabilitation, and thermal therapy (e.g., muscle pain relief, minimization of adverse effects of concussions, and others). Although the systems operate at nearly ideal efficiency, further improvements may be possible through reductions in thermal mass, enhancements in evaporative cooling power, and increases in the efficiency of thermal barrier switching. Integration with arrays of haptic actuators represents another promising direction for future work.

Materials and Methods

Fabricating the Electronics. Eagle computer-aided design (CAD) version 9.6.2 (Autodesk) served as the basis for generating schematics and layouts for the fPCBs. An ISO 9001-compliant PCB manufacturer produced fPCBs that consisted of a layer of polyimide (PI; 25 μm thick) with patterned Cu traces (Cu; 18 μm thick) on the top and bottom surfaces, each encapsulated with an insulating PI layer (12.5 μm thick) bonded with a silicone adhesive (12 μm thick). The fPCB was cut into the shape of a circle (radius: 125 mm), with serpentine (1 mm wide, 3.32 mm in initial end-to-end length, and 220° in arc angle) structures that connected square islands (16 × 16 mm^2 for each island) to support mechanical compliance. Each island contained a fractal-shaped Cu trace as a Joule heating element (area of the fractal occupies 14.4 × 14.4 mm^2). Each serpentine supported four 177-μm-wide Cu traces separated by 89.5 μm, on both sides. Various surface-mounted components, including Bluetooth Low Energy system-on-a-chip (BLE SoC; ISP1807-LR-RS, Insight SIP), analog-to-digital converters (ADC; MAX11617EEE+, Analog Devices Inc./Maxim Integrated), full-bridge rectifier (BAS4002ARPPE6327HTSA1, Infineon Technologies), voltage regulators (NCP114ASN330T1G and NCV8187AMT330TAG, onsemi), DC–DC converter (LM5166XDRCR, Texas Instruments), and 3.7-V lithium polymer battery charge management controller (MCP73831T-4ADI/OT, Microchip Technology), slide switch (CJS-1201TA, NIDEC COPAL ELECTRONICS), NTC thermistor (ERT-J0EV104FM, Panasonic Electronic Components), and passive components (resistors, capacitors, and inductors) bonded onto the fPCB with a low-temperature

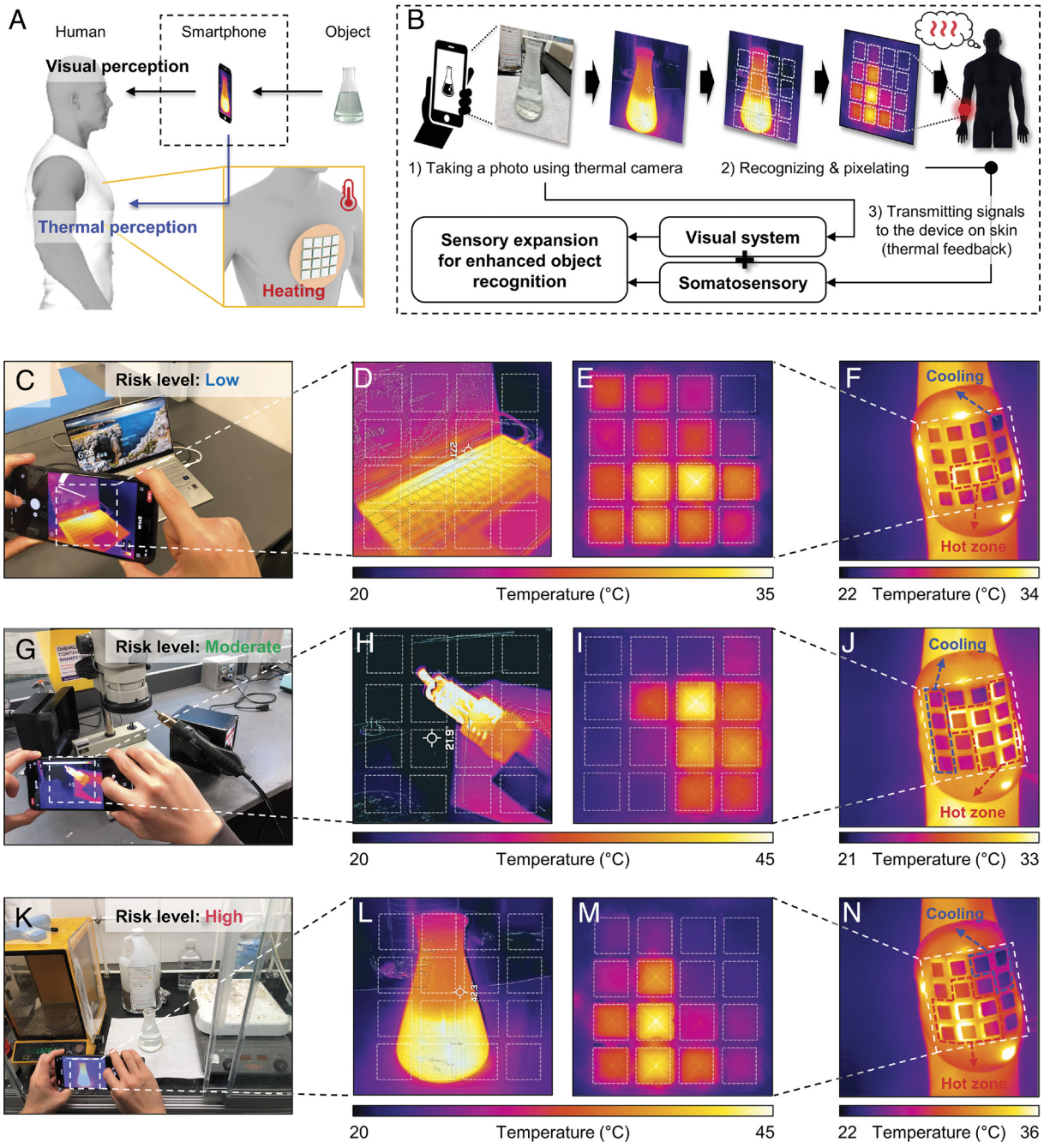

Fig. 6. Sensory expansion for thermal recognition of remote objects. (*A*) Conceptual illustration of remote thermal recognition using input from a mobile IR camera. (*B*) Flow chart for enhanced object recognition through automated pixelation and transmission of temperature information. (*C*) Photograph of an overheating laptop. (*D–F*) Corresponding IR image (*D*), device with associated thermal feedback (*E*), and thermal interface of a device on the forearm (*F*). (*G*) Photograph of a soldering station. (*H–J*) Corresponding IR image (*H*), device with associated thermal feedback (*I*), and thermal interface of the device on the forearm (*J*). (*K*) Photograph of an exothermic chemical reaction (H_2SO_4 + H_2O_2) in a flask. (*L–N*) Corresponding IR image (*L*), device with associated thermal feedback (*M*), and thermal interface of the device on the forearm (*N*). The IR images in (*E, I, M,*) show heater-facing images, and those in (*F, J, N,*) show cooling gel-facing images, respectively.

reflow process using soldering paste (TS391LT, Chip Quik) and a soldering heat gun (AOYUE Int866).

Encapsulating the System. A soft silicone-based material (Silbione RTV4420, Elkem) mixed with 5.0 wt.% of white pigment and 2.5 wt.% of light flesh tone pigment (Silc PigTM, Smooth-On) formed the top and bottom encapsulation layers by molding and curing at 80 °C. Top and bottom aluminum molds for this process resulted from machining with a three-axis milling machine (Modela Pro II MDX 540, Roland DGA). The encapsulation process involved placing the bottom encapsulation layer on the bottom aluminum mold, mounting the fPCB with electronics components on this layer, then covering the top encapsulation layer and bonding the assembly with uncured silicone elastomer in an orientation to align the heaters with the openings. After curing overnight at room temperature, a custom die tool (Millennium Die) cut away the center regions of top and bottom encapsulation layers to allow placement of cooling gels and STB structures. Removing the excess encapsulation layers completed the fabrication.

Integrating Cooling Gels with STBs. The thermal modules adopted a trilayer structure consisting of a cooling gel, an STB, and a Joule heater on the fPCB (from top to bottom). A commercial cooling gel sheet (BeKOOOL, Kobayashi) cut using a CO_2 laser (Universal Laser Systems, ULS) defined rectangular elements with sizes of 12.7 × 12.7 mm^2. The bladders used thin films of metallized EVOH

(EVALTM film; VM-XL, 12 μm thick, Kuraray) sealed at their perimeter edges using a thermal process. Before complete sealing, 30 μL 1-methoxyheptafluoropropane ($C_3F_7OCH_3$)-based engineered fluid (Novec 7000, 3M) with a low-boiling point (bp of 34 °C at 1 atm) was introduced using a 1-mL syringe. A medical-grade acrylate adhesive (1524, 3M, thickness of 60 μm) bonded the resulting STB to the bottom side of the heater (top side of the heater faces the skin). The cooling gel adhered to the bottom side of the STB (top side of the bladder faces the heater).

Measuring the Performance of the Thermal Module. The setup for measuring heating/cooling performance is shown in *SI Appendix*, Figs. S18 and S19. A water tank made of clear round wide-mouth plastic jar (ULINE, S-12753B-W, 70 mm dia.) provided temperature control for a 6 mm-thick slab of polydimethylsiloxane (PDMS) [Sylgard 184, mixing ratio with curing agent is 10:1 (w:w)] that served as the skin phantom model. A Kapton heater (70 mm dia.) and a waterproof negative temperature coefficient (NTC) sensor built inside the water tank electrically connected to a waterproof, electronic temperature control module switch with 10 A, 1-channel relay (W1209, HiLetgo) placed outside the tank. Switching the heater on and off maintained the temperature of the water in the tank to a desired value to regulate the temperature of the top surface of the PDMS to ~32 °C. Measurements of performance involved placing the thermal module onto the top surface of the PDMS. An NTC thermistor located between the Joule heater and the STB recorded the temperature of the thermal module upon heating/cooling through a serial monitor window in an Arduino (Windows Store 1.8.57.0). An ADC converted analog signals from the NTC thermistor to digital values (temperature values). A PID system controlled the heating power to reach and maintain a target temperature. A Power Profiler Kit II (PPK2) board (nRF-PPK2, Nordic Semiconductor) measured the applied current. A PPK2 board connected to a computer with a PPK application (nRF Connect) provided a real-time display of the current. Voltages between 0 and 5.0 V were selected through the PPK application. Values above 5.0 V were realized with an external DC power supply (MDC02, Tacklife). The heating power was calculated from the current and the voltage according to P = I × V. Based on these results, the expected lifetime of a typical battery (LiPo battery, 602530, 500 mAh) is 2.5 h for operation that involves a single thermal module set to 40 °C for the case that the temperature and *RH* of the air distant from the cooling gel are 22 °C and 45 %, respectively.

Modeling the Heat and Mass Transfer Balance to Determine the Convective Heat Transfer Coefficient. The steady-state, specific cooling power of the cooling gel followed from measurements of the skin temperature (T_{skin}), the gel temperature (T_{gel}), and the time rate of change of the mass of the gel ($\dot{m}$). The temperature of the ambient air and the *RH* in our laboratory were 22 °C and 45 %, respectively. Air convection near the cooling gel was free convection (airflow velocity, $v_{air} = 0$ m s^{-1}) under an ambient condition and forced convection ($v_{air} > 0$ m s^{-1}) when operating a fan.

For free convection ($v_{air} = 0$ m s^{-1}), the convective heat transfer coefficient (h_{air}) [W m^{-2} K^{-1}] can be calculated using the following relationships:

$$h_{air} = Nu \times \frac{k}{L}, \quad [1]$$

$$Nu = 0.54(Gr \times Pr)^{1/4}, \quad [2]$$

$$Gr = \frac{L^3 \rho^2 \beta g \Delta T}{\mu^2}, \quad [3]$$

$$Pr = \frac{C_p \mu}{k}, \quad [4]$$

where *Nu* is Nusselt number, a function of the Grashof number (*Gr*) and Prandtl number (*Pr*), *k* is the thermal conductivity of air [W m^{-1} K^{-1}], *L* is the lateral size of the cooling gel [m], ρ is the density of air [kg m^{-3}], β is the coefficient of thermal expansion, given by $1/T_{air}$ [K^{-1}], *g* is the gravitational acceleration [9.81 m s^{-1}], ΔT is the temperature difference between the cooling gel and air [K], μ is the dynamic viscosity of air [kg m^{-1} s^{-1}], and C_p is the specific heat capacity of air [J kg^{-1} K^{-1}].

For forced convection ($v_{air} > 0$ m s^{-1}), h_{air} can be calculated by solving the conservation of mass, momentum, and energy equations in conjunction with the properties of the airflow (flow of fluid). This one-dimensional heat transfer problem can be assumed to be a 'fluid flow (airflow) over flat plate (top surface of the cooling gel)' (35), by assuming a 'no-slip' condition and the critical Reynolds number (Re_{cr}) as 5 × 10^5.

$$h_{air} = Nu \times \frac{k}{L} = 0.664 \times Re_L^{0.5} Pr^{1/3}, \quad [5]$$

$$Re_L = \frac{v_{air} L}{\nu}, \quad [6]$$

$$T_{top} = \frac{T_{gel} + T_{air}}{2}, \quad [7]$$

where Re_L is Reynolds number for the cooling gel (with $L = 0.015$ m), v_{air} is the airflow velocity [m s^{-1}], ν is kinematic viscosity of the air [m^2 s^{-1}], T_{top} is the temperature at the interface of the cooling gel and the air [K], T_{gel} is temperature of the cooling gel [K], and T_{air} is the temperature of the airflow [K]. All calculated values for determining the specific cooling power of the cooling gel are listed in *SI Appendix*, Tables S2–S5.

Simulating the Behaviors of the STB. The 3D FEA model for the STB used a commercial software package (COMSOL Multiphysics 5.6.0). Fully coupled multiphysics modules for heat transfer and solid mechanics solved for the temperature distributions, the mechanical deformations, and the bladder expansion. The thin aluminized EVOH films (12 μm thick) were modeled by calculating plane stresses in the in-plane and out-of-plane directions of the film. The thermal and mechanical properties of materials used in the model are summarized in *SI Appendix*, Table S1. The thermophysical properties of Novec 7000 were obtained by referring to the reference fluid thermodynamic and transport properties database (REFPROP) developed by the National Institute of Standards and Technology shown in *SI Appendix*, Figs. S3 and S6. For simplicity, the simulations considered a Cu/PI composite with effective thermal and mechanical properties of the Peano-fractal shaped heater (Cu/PI) determined by an independent FEA model consisting of Cu traces embedded in PI shown in *SI Appendix*, Figs. S30–S32. The effective heat capacity and density are average properties weighted by the mass of Cu and PI. The effective thermal conductivity and elastic modulus correspond to estimates using the differential effective medium approximation (36) and calibrated by simulating the Cu traces embedded in PI. The cooling gel, as a mixture of polymer and water, has effective thermophysical properties estimated by composition (37) and a cooling capacity between 100 and 300 W m^{-2} K^{-1} (38). To solve for the temperature profile, the empirical power consumption of the heater was applied in the model as a volumetric heat source. The bottom temperature of the skin phantom was fixed according to the experimental heating source temperature. The top surface of the system involved natural convection to the ambient air. To solve for the deformation, the inner pocket pressure as a function of temperature as shown in *SI Appendix*, Fig. S3 was applied to expand the bladder. The bottom of the skin phantom was a fixed constraint, and the other surfaces of the system were free to move due to expansion. Along with the deformation, a moving mesh was updated at each time step.

Defining BLE Protocols, Software Control Strategies, and System Operation. The system used a BLE 5 SoC (ISP 1807). Temperature data from 16 thermal modules measured with a resolution of 12 bits every 0.5 s were transmitted to an iPad or iPhone through general Bluetooth communication protocols. The transmitted temperature information was stored in the cloud in the form of a NoSQL database using the Firebase Real-Time Database service. The updated temperature information was confirmed on the other mobile device connected to the cloud server, enabling multidevice temperature information sharing. The set point in the graphical user interface was transmitted to the system through Bluetooth, and the difference between the set point and the measured temperature of each module was monitored every 0.5 s. The temperature of the actuator was controlled by changing the duty cycle of the 1 kHz frequency pulse.

Human Subject Testing of Discriminability of Thermal Stimuli. The experimental protocols were approved by the Institutional Review Board of Northwestern University (STU00214800). All participants provided their consent before the tests. Healthy adult volunteers (age 30 to 36 y; four male and one female healthy individuals) performed the tests for measuring discriminability of spatially summated

thermal stimuli with no additional human-participant risk, following the provided study guidelines. Thermal stimulation was delivered by a device mounted on the forearm.

Demonstrating Operation in On-Body Thermoregulation. On-body thermoregulation capabilities were demonstrated under two weather conditions: i) cold weather (T_{air} ~ 13 °C), and ii) hot weather (T_{air} ~ 35 °C). The device on the right arm was operated by PID control for thermoregulation (set point is 32 °C). The device on the left arm was used only for sensing. Body movements both indoor/outdoor included sitting and walking. The temperature of the ambient air (T_{air}) was monitored with a digital thermometer (PerfectPrime, TC0521).

Delivering and Sensing Spatiotemporal Thermal Sensations for Remote Interactions. The demonstrations involved two devices, one at location 1 and the other at location 2 (distance between the two locations ~20 km). The device at location 1 was activated to produce a spatiotemporal temperature distribution in a pattern defined by touch with human fingers. At the same time, at location 2, the temperature information transmitted from the device at location 1 to the device at location 2 was detected using an IR camera (FLIR Systems, a6255sc). At 60, 120, and 180 s, three different temperature patterns were stimulated by touch, applied for several tens of seconds and then released. The temperature profile for each thermal module on the device at location 2 was recorded using an IR camera.

Recognizing Thermal Attributes of Remote Objects. A 160 × 120-pixel thermal image was collected using a mobile IR camera (FLIR ONE pro, FLIR Inc.), stored in the local memory of an iPhone and then divided into 4 × 4 regions each composed of 40 × 30 pixels. The average RGB value for each region was matched to the inferno color map and converted to an average temperature. The resulting information defined set point for a corresponding collection of thermal modules through BLE communication.

Data, Materials, and Software Availability. All study data are included in the article and/or *SI Appendix*.

ACKNOWLEDGMENTS. The work was supported by the Querrey Simpson Institute for Bioelectronics at Northwestern University. M.P acknowledges support from Basic Science Research Program through the National Research Foundation of Korea (NRF) funded by the Ministry of Education (2020R1A6A3A03037287). Y.H.J. acknowledges support from the National Research Foundation of Korea grant funded by the Korean Government (Ministry of Science and ICT) (no. 2022R1C1C1003994).

Author affiliations: [a]Querrey-Simpson Institute for Bioelectronics, Northwestern University, Evanston, IL 60208; [b]Department of Mechanical Science and Engineering, University of Illinois Urbana-Champaign, Urbana, IL 61801; [c]Department of Electronic Engineering, Hanyang University, Seoul 04763, Republic of Korea; [d]Department of Mechanical Engineering, Northwestern University, Evanston, IL 60208; [e]Department of Materials Science and Engineering, Northwestern University, Evanston, IL 60208; [f]Department of Biomedical Engineering, Northwestern University, Evanston, IL 60208; and [g]Department of Neurological Surgery, Feinberg School of Medicine, Northwestern University, Chicago, IL 60611

Author contributions: M.P. and J.A.R. designed research; M.P., J.-Y.Y., T.Y., Y.H.J., A.V.-G., J.-H.K., J.S., W.-Y.M., G.L., S.Y., H.L., J.-T.K., H.-S.S., M.T.F., H.-J.Y., N.M., Y.H., and W.P.K. performed research; M.P., J.-Y.Y., T.Y., Y.H.J., S.L., and W.P.K. analyzed data; and M.P., J.-Y.Y., T.Y., and J.A.R. wrote the paper.

1. M. J. Caterina *et al.*, The capsaicin receptor: A heat-activated ion channel in the pain pathway. *Nature* **389**, 816–824 (1997).
2. D. D. Mckemy, W. M. Neuhausser, D. Julius, Identification of a cold receptor reveals a general role for TRP channels in thermosensation. *Nature* **416**, 52–58 (2002).
3. X. Yu *et al.*, Skin-integrated wireless haptic interfaces for virtual and augmented reality. *Nature* **575**, 473–479 (2019).
4. Y. H. Jung, J.-H. Kim, J. A. Rogers, Skin-integrated vibrohaptic interfaces for virtual and augmented reality. *Adv. Funct. Mater.* **31**, 2008805 (2021).
5. Y. H. Jung *et al.*, A wireless haptic interface for programmable patterns of touch across large areas of the skin. *Nat. Electron.* **5**, 374–385 (2022).
6. S. S. Gharat, "Vibro-thermal haptic display for socio-emotional communication through pattern generations," Doctoral dissertation, (Arizona State University Electronic Theses and Dissertations, Tempe, AZ, 2021).
7. J. Tewall, J. Bird, G. R. Buchanan, "Heat-Nav: Using temperature changes as navigational cues" in *Proceedings of the 2017 CHI Conference on Human Factors in Computing Systems*, (Association for Computing Machinery, New York, NY, 2017), pp. 1131–1135.
8. J. Lee *et al.*, Stretchable skin-like cooling/heating device for reconstruction of artificial thermal sensation in virtual reality. *Adv. Funct. Mater.* **30**, 1909171 (2020).
9. D. Kim *et al.*, Highly stretchable and oxidation-resistive Cu nanowire heater for replication of the feeling of heat in a virtual world. *J. Mater. Chem. A* **8**, 8281–8291 (2020).
10. K. Zhu, S. Perrault, T. Chen, S. Cai, R. L. Peiris, A sense of ice and fire: Exploring thermal feedback with multiple thermoelectric-cooling elements on a smart ring. *Int. J. Hum. Comput.* **130**, 234–247 (2019).
11. S. Song, "Hot & tight: Exploring thermo and squeeze cues recognition on wrist wearables" in *Proceedings of the 2015 ACM International Symposium on Wearable Computers*, (Association for Computing Machinery, New York, NY, 2015), pp. 39–42.
12. S. Cai, P. Ke, T. Narumi, K. Zhu, "ThermAirGlove: A pneumatic glove for thermal perception and material identification in virtual reality" in *2020 IEEE Conference on Virtual Reality and 3D User Interfaces (VR)*, (IEEE, Atlanta, GA, 2020), pp. 248–257.
13. A. Nasser, K. Zheng, K. Zhu, "ThermEarhook: Investigating spatial thermal haptic feedback on the auricular skin area" in *Proceedings of the 2021 International Conference on Multimodal Interaction*, (Association for Computing Machinery, New York, NY, 2021), pp. 662–672.
14. T. Maeda, T. Kurahashi, "TherModule: Wearable and modular thermal feedback system based on a wireless platform" in *Proceedings of the 10th Augmented Human International Conference 2019*, (Association for Computing Machinery, New York, NY, 2019), pp. 1–8.
15. D. Jain, "Immersive scuba diving simulator using virtual reality" in *Proceedings of the 29th Annual Symposium on User Interface Software and Technology* (2016), (Association for Computing Machinery, New York, NY, 2016), pp. 729–739.
16. M. Luo *et al.*, High-density thermal sensitivity maps of the human body. *Build. Environ.* **167**, 106435 (2020).
17. L. A. Jones, M. Berris, "The psychophysics of temperature perception and thermal-interface design" in *Proceedings 10th Symposium on Haptic Interfaces for Virtual Environment and Teleoperator Systems. HAPTICS 2002*, (IEEE, Orlando, FL, 2002), pp. 137–142.
18. W. S. Cain, Spatial discrimination of cutaneous warmth. *Am. J. Psychol.* **86**, 169–181 (1973).
19. E. H. Weber, *The Sense of Touch* (translated from De Tactu by E. H. Weber 1834) (Academic Press, New York, 1834), p. 278.
20. J. D. Hardy, T. W. Oppel, Studies in temperature sensation. III. The sensitivity of the body to heat and the spatial summation of the end organ responses. *J. Clin. Investig.* **16**, 533–540 (1937).
21. D. R. Kenshalo, T. Decker, A. Hamilton, Spatial summation on the forehead, forearm, and back produced by radiant and conducted heat. *J. Comp. Physiol.* **63**, 510–515 (1967).
22. K. Parida, H. Bark, P. S. Lee, Emerging thermal technology enabled augmented reality. *Adv. Funct. Mater.* **31**, 2007952 (2021).
23. D. C. Spray, Cutaneous temperature receptors. *Ann. Rev. Physiol.* **48**, 625–638 (1986).
24. R. A. Kishore, A. Nozariasbmarz, B. Poudel, M. Sanghadasa, S. Priya, Ultra-high performance wearable thermoelectric coolers with less materials. *Nat. Commun.* **10**, 1–13 (2019).
25. S. Hong *et al.*, Wearable thermoelectrics for personalized thermoregulation. *Sci. Adv.* **5**, eaaw0536 (2019).
26. S. Ferber *et al.*, Evaporative cooling hydrogel packaging for storing biologics outside of the cold chain. *Adv. Healthc. Mater.* **7**, 1800220 (2018).
27. M. Misumi, M. Yamashita, "Adhesive cooling composition and process for its preparation." U.S. Patent No. 6,524,612 (2003).
28. J. A. Fan *et al.*, Fractal design concepts for stretchable electronics. *Nat. Commun.* **5**, 1–8 (2014).
29. H. Hensel, "Cutaneous thermoreceptors" in *Handbook of Sensory Physiology, Volume 2: Somatosensory System*, A. Iggo, Eds. (Springer-Verlag, 1973), p. 81.
30. M. Zamengo, J. Morikawa, Evaluation of cooling ability for a novel heat sink made of polyvinyl alcohol hydrogel. *Int. J. Heat Mass Transf.* **143**, 118523 (2019).
31. E. V. Osilla, J. L. Marsidi, S. Sharma, *Physiology, Temperature Regulation* (StatPearls Publishing, 2018).
32. Y. Jung *et al.*, Soft multi-modal thermoelectric skin for dual functionality of underwater energy harvesting and thermoregulation. *Nano. Energy* **95**, 107002 (2022).
33. A. E. Ali, "ThermalWear: Exploring wearable on-chest thermal displays to augment voice messages with affect" in *Proceedings of the 2020 CHI Conference on Human Factors in Computing systems* (2020), (Association for Computing Machinery, New York, NY, 2020), pp. 1–14.
34. G. Wilson, S. Brewster, M. Halvey, S. A. Hughes, "Thermal Icons: Evaluating structured thermal feedback for mobile interaction" in *Proceedings of the 14th International Conference on Human-Computer Interaction with Mobile Devices and Services* (2012), (Association for Computing Machinery, New York, NY, 2012), pp. 309–312.
35. R. B. Bird, Transport phenomena. *Appl. Mech. Rev.* **55**, R1–R4 (2002).
36. S. Torquato, *Random Heterogeneous Materials* (Springer Science + Business Media, LLC, 2001).
37. S. Pu *et al.*, Bioinspired sweating with temperature sensitive hydrogel to passively dissipate heat from high-end wearable electronics. *Energy Convers. Manag.* **180**, 747–756 (2019).
38. S. Cui *et al.*, Cooling performance of bio-mimic perspiration by temperature-sensitive hydrogel. *Int. J. Therm. Sci.* **79**, 276–282 (2014).